EPJ manuscript No.
(will be inserted by the editor)

Kaonic production of $\Lambda(1405)$ off deuteron target in chiral dynamics

D. Jido[1], E. Oset[2], and T. Sekihara[3]

[1] Yukawa Institute for Theoretical Physics, Kyoto University, Kyoto 606-8502, Japan
[2] Departamento de Física Teórica and IFIC, Centro Mixto Universidad de Valencia-CSIC, Institutos de Investigación de Paterna, Aptdo. 22085, 46071 Valencia, Spain
[3] Department of Physics, Graduate School of Science, Kyoto University, Kyoto, 606-8502, Japan

Received: date / Revised version: date

Abstract. The K^- induced production of $\Lambda(1405)$ is investigated in $K^-d \to \pi\Sigma n$ reactions based on coupled-channels chiral dynamics, in order to discuss the resonance position of the $\Lambda(1405)$ in the $\bar{K}N$ channel. We find that the $K^-d \to \Lambda(1405)n$ process favors the production of $\Lambda(1405)$ initiated by the $\bar{K}N$ channel. The present approach indicates that the $\Lambda(1405)$ resonance position is 1420 MeV rather than 1405 MeV in the $\pi\Sigma$ invariant mass spectra of $K^-d \to \pi\Sigma n$ reactions. This is consistent with an observed spectrum of the $K^-d \to \pi^+\Sigma^- n$ with 686-844 MeV/c incident K^- by bubble chamber experiments done in the 70's. Our model also reproduces the measured $\Lambda(1405)$ production cross section.

Key words. Structure of $\Lambda(1405)$ – Kaon induced production of $\Lambda(1405)$ – Chiral unitary model

PACS. 14.20.Jn Hyperons – 25.80.Nv Kaon-induced reactions – 13.75.Jz Kaon-baryon interactions – 12.39.Fe Chiral Lagrangians

1 Introduction

The structure of the $\Lambda(1405)$ resonance is an important recent issue particularly to understand $\bar{K}$-nucleus interactions. The $\Lambda(1405)$ has been a historical example of a dynamically generated resonance in meson-baryon coupled-channels dynamics with $S = -1$ [1]. Modern investigations based on chiral dynamics with a unitary framework also reproduce well the observed spectrum of the $\Lambda(1405)$ together with cross sections of K^-p to various channels [2, 3, 4, 5, 6, 7]. Recently it was pointed out in Ref. [8] that the $\Lambda(1405)$ can be regarded almost purely as a dynamically generated state in meson-baryon scattering, while the description of the $N(1535)$ demands some components other than meson-baryon ones, such as genuine quark components.

One of the important consequences of chiral dynamics is that the $\Lambda(1405)$ is described by superposition of two resonance states [9]. One state located around 1420 MeV couples dominantly to the $\bar{K}N$ channel, while the other one sitting around 1390 MeV with a 130 MeV width couples strongly to the $\pi\Sigma$ channel. Consequently, the spectra of the $\Lambda(1405)$ depend on the channels and the resonance position in the $\bar{K}N$ channel is 1420 MeV, higher than the nominal one which is 1405 MeV. Therefore, it is important to observe the resonance position of the $\Lambda(1405)$ in the $\bar{K}N$ channel.

To observe the resonance position of the $\Lambda(1405)$ in the $\bar{K}N$ channel it is necessary to produce the $\Lambda(1405)$ by reactions initiated by $\bar{K}N$. Since the $\Lambda(1405)$ resonance appears below the threshold of the $\bar{K}N$ channel, direct production of $\Lambda(1405)$ in the $\bar{K}N$ channel is kinematically forbidden. This fact leads us to indirect productions of $\Lambda(1405)$, such as $\gamma p \to \Lambda(1405)K^*$ [10], $K^-p \to \gamma\Lambda(1405)$ [11], $K^-p \to \pi_0\Lambda(1405)$ [12,13], and nuclear reactions [14]. Here we discuss the K^- induced production of $\Lambda(1405)$ with a deuteron target, $K^-d \to \Lambda(1405)n$. In this reaction, the final neutron takes energy out from the initial kaon and the $\Lambda(1405)$ is produced by the $\bar{K}N$ channel.

The paper is organized as follows: In Sec. 2, we explain our model to calculate the $K^-d \to \pi\Sigma n$ reactions and introduce the description of $\Lambda(1405)$ based on the chiral unitary approach. In Sec. 3 we show our numerical results of the calculations and compare our results with experiments. Section 4 is devoted to a summary of this work.

2 Formulation

In this section, we explain our approach to calculate the cross section of the $K^-d \to \pi\Sigma n$ reaction. In Sec. 2.1, we discuss the kinematics of this reaction and introduce

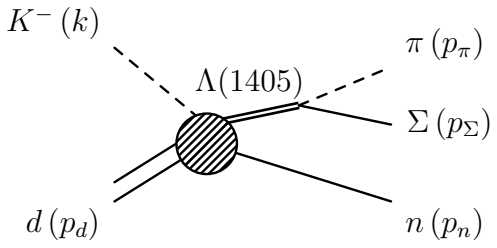

Fig. 1. Kinematics of the $K^- d \to \pi\Sigma n$.

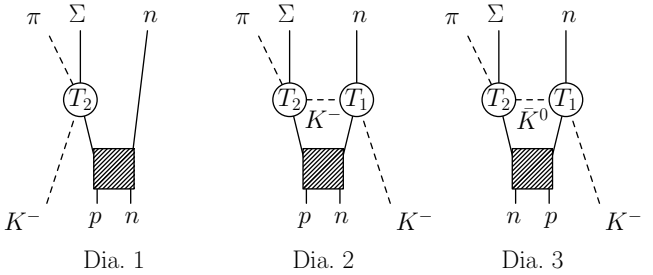

Fig. 2. Diagrams for the calculation of the $K^- d \to \pi\Sigma n$ reaction. T_1 and T_2 denote the scattering amplitudes for $\bar{K}N \to \bar{K}N$ and $\bar{K}N \to \pi\Sigma$, respectively.

relevant diagrams for the $\Lambda(1405)$ production. The T-matrix is calculated in Sec. 2.2. The description of the two-body meson-baryon scattering amplitudes and the model of $\Lambda(1405)$ in the chiral unitary approach are discussed in Sec. 2.3.

2.1 Kinematics

We consider $\Lambda(1405)$ production induced by K^- with a deuteron target, $K^- d \to \Lambda(1405) n$. The $\Lambda(1405)$ produced in this reaction decays into $\pi\Sigma$ with $I = 0$ as shown in Fig. 1. The $\Lambda(1405)$ is identified by the $\pi\Sigma$ invariant mass spectra of this reaction. Figure 1 also gives the kinematical variables of the initial and final particles. The kinematics of the three-body final state is completely fixed by five variables, the $\pi\Sigma$ invariant mass $M_{\pi\Sigma}$, the neutron solid angle Ω_n in the c.m. frame and the pion solid angle Ω_π^* in the rest frame of π and Σ [15]. Thus the differential cross section of this reaction can be written by

$$d\sigma = \frac{1}{(2\pi)^5} \frac{M_d M_\Sigma M_n}{4 k_{\rm c.m.} E_{\rm c.m.}^2} |\mathcal{T}|^2 |\boldsymbol{p}_\pi^*|\, |\boldsymbol{p}_n|\, dM_{\pi\Sigma} d\Omega_\pi^* d\Omega_n \quad (1)$$

where $\mathcal{T}$ is the T-matrix of this reaction, $E_{\rm c.m.}$ is the center of mass energy, $k_{c.m.}$ is the kaon c.m. momentum and $\boldsymbol{p}_\pi^*$ is the pion momentum in the rest frame of π and Σ. The pion momentum $|\boldsymbol{p}_\pi^*|$ in the $\pi\Sigma$ rest frame can be fixed by the invariant mass $M_{\pi\Sigma}$ as

$$|\boldsymbol{p}_\pi^*| = \frac{\lambda^{1/2}(M_{\pi\Sigma}^2, m_\pi^2, M_\Sigma^2)}{2 M_{\pi\Sigma}} \quad (2)$$

with the Källen function $\lambda(x,y,z) = x^2 + y^2 + z^2 - 2xy - 2yz - 2zx$.

The $\Lambda(1405)$ production is investigated by limiting the kinematics with the invariant mass of the final $\pi\Sigma$ state around 1350 to 1450 MeV, in which the resonating $\pi\Sigma$ forms the $\Lambda(1405)$ and the resonance contribution may dominate the cross section. Thus, we do not consider the diagrams in which the final π and Σ are emitted from different vertices, since they are not correlated. In this $\Lambda(1405)$ dominance approximation, we have three diagrams for this reaction as shown in Fig. 2. The left diagram of Fig. 2 expresses the $\Lambda(1405)$ production in the impulse approximation. We refer to this diagram as direct production process. The middle and right diagrams are for two-step processes with $\bar{K}$ exchange. We refer to these diagrams as double scattering diagrams.

In Fig. 2, T_1 and T_2 denote s-wave scattering amplitudes of $\bar{K}N \to \bar{K}N$ and $\bar{K}N \to \pi\Sigma$, respectively. These amplitudes are calculated in coupled-channels approach based on chiral dynamics, as we will explain later. In the amplitude T_2, the $\Lambda(1405)$ resonance is involved. Note that, in these three diagrams, the $\Lambda(1405)$ in the amplitude T_2 is produced by the $\bar{K}N$ channel. For the amplitude T_1, the energies of interest are 1600 MeV to 1800 MeV for the K^- incident momenta 600 MeV/c to 1000 MeV/c in the lab. frame. We do not consider double scattering diagrams with pion exchanges in which Σ and π are emitted separately from the T_1 and T_2 amplitudes, respectively. Such diagrams may give smooth backgrounds in the $\pi\Sigma$ invariant mass spectra. We do not consider the $\Sigma(1385)$ resonance in the T_2 amplitude, since the branching rate of $\Sigma(1385)$ to $\pi\Sigma$ is only 12%.

For the energetic incident K^- with several hundreds MeV/c momentum in the lab. frame, the contribution of diagram 1 (direct production) is expected to be very small, since the $\Lambda(1405)$ is produced below the $\bar{K}N$ threshold by the energetic K^- and a far off-shell nucleon and the deuteron wavefunction has tiny component of such a far off-shell nucleon. In contrast to the direct production, in the double scattering diagrams, the large energy of the incident K^- is carried away by the final neutron and the exchanged kaon can have a suitable energy to create the $\Lambda(1405)$ colliding with the other nucleon in the deuteron.

2.2 Scattering amplitude

Let us calculate the T-matrix for the $K^- d \to \pi\Sigma n$ reaction. The T-matrix for the diagram 1 given in Fig. 2 can be calculated in the impulse approximation in which the incident K^- and the proton in the deuteron transform into $\pi\Sigma$ and the neutron behaves as a spectator of the reaction.

Letting the wavefunctions of the incident kaon and the particles in the final state be given by plane waves and writing the wavefunctions of the nucleons in the deuteron as φ_i $(i = 1, 2)$, we obtain the connected part of the S-

matrix:

$$S = \int d^4x_1\,(-i)T_{K^-p\to\pi\Sigma}\,\mathcal{N}_\Sigma e^{ip_\Sigma\cdot x_1}\mathcal{N}_\pi e^{ip_\pi\cdot x_1} \times \mathcal{N}_1\varphi_1(\boldsymbol{x}_1)e^{-ip_1^0x_1^0}\mathcal{N}_{K^-}e^{-ik\cdot x_1} \times \int d^3x_2\,\mathcal{N}_n e^{-i\boldsymbol{p}_n\cdot\boldsymbol{x}_2}\,\mathcal{N}_2\varphi_2(\boldsymbol{x}_2) \quad (3)$$

where $T_{K^-p\to\pi\Sigma}$ is the T-matrix for the $K^-p\to\pi\Sigma$, and p_1 and p_2 are the momenta of the proton and neutron inside the deuteron, respectively. The normalization factors of the wavefunctions are given by $\mathcal{N}_i=\sqrt{M_i/E_i}$ for baryons and $\mathcal{N}_a=1/\sqrt{2\omega_a}$ for mesons. The plane waves are normalized inside a box with a unit volume.

The integration of the time component x_1^0 give the delta function for energy conservation:

$$\int dx_1^0 e^{-i(k^0+p_1^0-p_\Sigma^0-p_\pi^0)x_1^0} = 2\pi\delta(k^0+p_1^0-p_\Sigma^0-p_\pi^0). \quad (4)$$

In the impulse approximation, the energy of the spectator neutron does not change, $p_2^0=p_n^0$. Taking the deuteron energy as the sum of the energies of the nucleons, $p_d^0=p_1^0+p_2^0$, we obtain the total energy conservation $k^0+p_d^0-p_\Sigma^0-p_\pi^0-p_n^0=0$. Here, in general, $p_n^0\neq p_2^0$. Thus one must assume in the impulse approximation that the initial energy in the deuteron is not equally distributed between the two nucleons.

To perform the spacial integrals, we introduce the relative coordinate for $\boldsymbol{x}_1$ and $\boldsymbol{x}_2$ as $\boldsymbol{R}=(\boldsymbol{x}_1+\boldsymbol{x}_2)/2$ and $\boldsymbol{r}=\boldsymbol{x}_1-\boldsymbol{x}_2$. We also introduce the deuteron wavefunction for the relative motion $\varphi(r)$ and assume that the center of mass motion of the deuteron is described as the plane wave. Namely we replace the nucleon wavefunctions, $\varphi_1(\boldsymbol{x}_1)$ and $\varphi_2(\boldsymbol{x}_2)$, as follows:

$$\mathcal{N}_1\mathcal{N}_2\varphi_1(\boldsymbol{x}_1)\varphi_2(\boldsymbol{x}_2)\to\mathcal{N}_d e^{i\boldsymbol{p}_d\cdot\boldsymbol{R}}\varphi(\boldsymbol{r}) \quad (5)$$

where the deuteron wavefunction is normalized as

$$\int d^3r|\varphi(\boldsymbol{r})|^2=1. \quad (6)$$

We neglect d-wave component of the deuteron wavefunction. The s-wave wavefunction $\varphi(r)$ in the rest frame of the deuteron is parametrized by analytic functions [16] as

$$\varphi(r)=\sum_{j=1}^{11}\frac{C_j}{r}\exp(-m_jr). \quad (7)$$

We use the parametrization for C_j and m_j given in Ref. [23]. The integration in terms of $\boldsymbol{R}$ gives the delta function for total momentum conservation, while the integration of $\boldsymbol{r}$ gives the Fourier transformation of the deuteron wavefunction:

$$\int d^3r\varphi(r)\,e^{i(\boldsymbol{k}+\boldsymbol{p}_n-\boldsymbol{p}_\Sigma-\boldsymbol{p}_\pi)\cdot\frac{\boldsymbol{r}}{2}}=\tilde{\varphi}(\boldsymbol{p}_n-\frac{\boldsymbol{p}_d}{2}) \quad (8)$$

where we have used momentum conservation.

Finally we obtain the S-matrix for the diagram 1 as

$$S = -iT_{K^-p\to\pi\Sigma}\,\varphi(\boldsymbol{p}_n-\frac{\boldsymbol{p}_d}{2})\,\mathcal{N}_d\mathcal{N}_K\mathcal{N}_\Sigma\mathcal{N}_\pi\mathcal{N}_n \times(2\pi)^4\delta^4(p_d+k-p_\Sigma-p_\pi-p_n). \quad (9)$$

Since the T-matrix is given by $S=1-i(2\pi)^4\delta^4(p_d+k-p_\Sigma-p_\pi-p_n)\,(\prod_i\mathcal{N}_i)\,\mathcal{T}$, we obtain the T-matrix for the diagram 1 as

$$\mathcal{T}_1=T_{K^-p\to\pi\Sigma}(M_{\pi\Sigma})\,\varphi(\boldsymbol{p}_n-\frac{\boldsymbol{p}_d}{2}). \quad (10)$$

Next let us consider the double scattering diagrams shown as diagrams 2 and 3 in Fig. 2. In the same way as the calculation of diagram 1, the connected S-matrix for diagram 2 is obtained as

$$S = (\prod_i\mathcal{N}_i)\int d^4x_1\int d^4x_2\,(i)\int\frac{d^4q}{(2\pi)^4}\frac{e^{-iq\cdot(x_1-x_2)}}{q^2-m_K^2+i\epsilon} \times e^{ip_\Sigma\cdot x_1}e^{ip_\pi\cdot x_1}e^{ip_n\cdot x_2}e^{-ik\cdot x_2}e^{-ip_1^0x_1^0}\varphi_1(\boldsymbol{x}_1) \times e^{-ip_2^0x_2^0}\varphi_2(\boldsymbol{x}_2)(-i)T_{K^-n\to K^-n}\,(-i)T_{K^-p\to\pi\Sigma}. \quad (11)$$

The integrations with respect to x_1^0 and x_2^0 give energy conservation $p_1^0+q^0=p_\Sigma^0+p_\pi^0$ and $p_2^0+k^0=q^0+p_n^0$, respectively. Integrating with respect to q_0

$$\int\frac{dq^0}{2\pi}2\pi\delta(p_1^0+q^0-p_\Sigma^0-p_\pi^0)2\pi\delta(p_2^0+k^0-q^0-p_n^0) = 2\pi\delta(k^0+p_d^0-p_\Sigma^0-p_\pi^0-p_n^0) \quad (12)$$

we obtain total energy conservation and q^0 has been fixed as $q^0=k^0+p_2^0-p_n^0=p_\Sigma^0+p_\pi^0-p_1^0$. Here we have used again $p_1^0+p_2^0=p_d^0$. Introducing again the relative coordinate for $\boldsymbol{x}_1$ and $\boldsymbol{x}_2$ and the deuteron wavefunction as Eq. (5), we find that the integration with respect to $\boldsymbol{R}$ gives total momentum conservation and that the integration of $\boldsymbol{r}$ provides the Fourier transformation of the deuteron wavefunction:

$$\int d^3r\,\varphi(r)\,e^{i(-\boldsymbol{k}+\boldsymbol{p}_n-\boldsymbol{p}_\Sigma-\boldsymbol{p}_\pi+2\boldsymbol{q})\cdot\frac{\boldsymbol{r}}{2}}=\tilde{\varphi}(\boldsymbol{q}+\boldsymbol{p}_n-\boldsymbol{k}-\frac{\boldsymbol{p}_d}{2})$$

with momentum conservation $\boldsymbol{p}_\Sigma+\boldsymbol{p}_\pi=\boldsymbol{p}_d+\boldsymbol{k}-\boldsymbol{p}_n$. Finally we obtain the T-matrix for diagram 2 as

$$\mathcal{T}_2=T_{K^-p\to\pi\Sigma}(M_{\pi\Sigma})\int\frac{d^3q}{(2\pi)^3}\frac{\tilde{\varphi}(\boldsymbol{q}+\boldsymbol{p}_n-\boldsymbol{k}-\frac{\boldsymbol{p}_d}{2})}{q^2-m_K^2+i\epsilon} \times T_{K^-n\to K^-n}(W_1)\ . \quad (13)$$

where W_1 denotes the invariant mass of the initial kaon and the neutron inside the deuteron, $W_1\equiv\sqrt{(k+p_2)^2}$. In principle, W_1 depends on the integral momentum $\boldsymbol{q}$ as $W_1=\sqrt{(k^0+p_2^0)^2-(\boldsymbol{q}+\boldsymbol{p}_n)^2}$, where we have used the momentum conservation $\boldsymbol{k}+\boldsymbol{p}_2=\boldsymbol{q}+\boldsymbol{p}_n$ at the vertex.

The variables q^0 and W_1 can be fixed by kinematics but depend on energies of the nucleons in the deuteron. To evaluate these values, let us take the deuteron rest

frame, that is, the laboratory frame. The deuteron is a loosely bound system of proton and neutron with about 2 MeV binding energy. Neglecting the binding energy for the neutron, we evaluate

$$q^0 = M_N + k^0 - p_n^0. \tag{14}$$

For the determination of W_1, we recall that the wavefunction of the nucleons inside the deuteron in momentum space has the largest component when the nucleon is almost at rest in the rest frame of the deuteron. Namely, in Eq. (13), the function $\tilde{\varphi}$ has the maximum at $\boldsymbol{q} = \boldsymbol{k} - \boldsymbol{p}_n$ in the lab. frame. This fact allows us to determine W_1 as

$$W_1 = \sqrt{(M_N + k^0)^2 - \boldsymbol{k}^2}. \tag{15}$$

Note that, under this assumption, the energy W_1 for the $K^- n \to K^- n$ amplitude is completely fixed by kinematics without depending on the momenta of the final state. Thus, the value of the $K^- n \to K^- n$ scattering amplitude contributes only to the absolute value of the cross section and does not provide any structure in the invariant mass spectra. We can estimate the deviation of W_1 from this approximation. The deuteron wavefunction φ has half of the maximum value at $|\boldsymbol{q} + \boldsymbol{p}_n - \boldsymbol{k}| = 45$ MeV in Eq. (13). With this momentum, at most, W can be change ± 20 MeV for the 800 MeV/c incident K^- momentum. We will discuss this approximation more in Sec. 3.2.5.

In the same way, we can calculate the T-matrix for diagram 3:

$$\mathcal{T}_3 = -T_{\bar{K}^0 n \to \pi\Sigma}(M_{\pi\Sigma}) \int \frac{d^3q}{(2\pi)^3} \frac{\tilde{\varphi}(\boldsymbol{q} + \boldsymbol{p}_n - \boldsymbol{k} - \frac{\boldsymbol{p}_d}{2})}{q^2 - m_K^2 + i\epsilon} \times T_{K^- p \to \bar{K}^0 n}(W_1)\ . \tag{16}$$

The negative sign in the right had side comes from the isospin configuration of the deuteron. Again W_1 is fixed by Eq. (15).

Finally, the total T-matrix is given by summing up these three amplitudes:

$$\mathcal{T} = \mathcal{T}_1 + \mathcal{T}_2 + \mathcal{T}_3 \tag{17}$$

where $\mathcal{T}_i$ $(i = 1, 2, 3)$ are given in Eqs. (10), (13) and (16), respectively. Note again that, in these amplitudes $\mathcal{T}_i$ $(i = 1, 2, 3)$, the $\Lambda(1405)$ is involved in the $\bar{K}N$-initiated amplitudes $T_{\bar{K}N \to \pi\Sigma}$.

We do not consider further multiple scattering since we are dealing with a deuteron break up process where the final baryons go apart from each other and are weakly correlated. Also the initial kaon energy is not small. This situation is very different from the coherent process of $\bar{K}d$ elastic scattering at threshold appearing in the evaluation of the $\bar{K}d$ scattering length. In this case the slow kaon sticks around the nucleons of the deuteron and multiple scattering with the two nucleons is needed in the evaluation of the scattering length [17,18,19,20]. The situation bears much resemblance to the case of elastic low energy pion nucleus scattering, which requires the full solution of the Klein-Gordon equation accounting for multiple scattering with the nucleons [21], and the quasielastic breakup processes which proceeds incoherently with the contribution of the first process kinemallically allowed [22].

2.3 Description of the $\bar{K}N$ scattering amplitudes and model for the $\Lambda(1405)$

For the description of the $\Lambda(1405)$, we use the chiral unitary approach, in which the $\Lambda(1405)$ is dynamically generated in coupled-channels of meson-baryon scattering with strangeness $S = -1$ and charge $Q = 0$, namely $K^- p$, $\bar{K}^0 n$, $\pi^0\Lambda$, $\pi^0\Sigma^0$, $\eta\Lambda$, $\eta\Sigma^0$, $\pi^+\Sigma^-$, $\pi^-\Sigma^+$, $K^+\Xi^-$ and $K^0\Xi^0$. The scattering amplitudes for the meson-baryon channels are obtained by solving the Bethe-Salpeter equation with the s-wave interaction kernels V given by chiral Lagrangian. The Bethe-Salpeter equation turns out to be an algebraic equation of the meson-baryon coupled channels if we consider elastic unitarity in the N/D method [4]:

$$T_{ij}(W) = V_{ij}(W) + V_{ik}(W) G_k(W) T_{kj}(W). \tag{18}$$

where i, j are the channel indices given in Ref. [3] and W denotes the center of mass energy.

In Eq. (18), V is given by the leading order of the chiral Lagrangian as

$$V_{ij}(W) = -\frac{C_{ij}}{4f^2}(2W - M_i - M_j) \left(\frac{M_i + E_i}{2M_i}\right)^{1/2} \left(\frac{M_j + E_j}{2M_j}\right)^{1/2} \tag{19}$$

with the baryon masses M_i and energy E_i. The coefficient C_{ij} in Eq. (19) is the channel coupling which is fixed by the flavor SU(3) group structure, and f is the decay constant of the meson in the chiral field $U = \exp[i\sqrt{2}\Phi/f]$. Here we use an averaged value of $f = 1.123 f_\pi$ with $f_\pi = 93$ MeV as done in Ref. [5] to deal with the $\bar{K}N$ interaction.

The diagonal matrix $G_k(W)$ in Eq. (18) is a meson-baryon loop function and is evaluated with dimensional regularization:

$$\begin{aligned} G_k(W) &= i \int \frac{d^4q}{(2\pi)^4} \frac{2M_k}{(P-q)^2 - M_k^2 + i\epsilon} \frac{1}{q^2 - m_k^2 + i\epsilon} \\ &= \frac{2M_k}{16\pi^2} \left\{ a_k(\mu) + \ln \frac{M_k^2}{\mu^2} + \frac{m_k^2 - M_k^2 + W^2}{2W^2} \ln \frac{m_k^2}{M_k^2} \right. \\ &\quad + \frac{\bar{q}_k}{W} \left[\ln(W^2 - (M_k^2 - m_k^2) + 2\bar{q}_k W) \right. \\ &\quad + \ln(W^2 + (M_k^2 - m_k^2) + 2\bar{q}_k W) \\ &\quad - \ln(-W^2 + (M_k^2 - m_k^2) + 2\bar{q}_k W) \\ &\quad \left. \left. - \ln(-W^2 - (M_k^2 - m_k^2) + 2\bar{q}_k W) \right] \right\} \end{aligned} \tag{20}$$

where m_i is the meson mass, $\bar{q}_i$ is the center of mass momentum and $a_i(\mu)$ is the subtraction constant with a renormalization scale μ. The subtraction constants are only the free parameters in this model and are determined so as to reproduce the threshold properties of $K^- p$ to several channels [2], which were obtained by K^- absorptions of Kaonic hydrogen [24]. In a recent work [8], it is found that the values of the subtraction constant are very important to determine the nature of the dynamically generated resonances in the chiral unitary approach. Here we take a standard parameter set given in Ref. [5]:

$$\begin{aligned} a_{\bar{K}N} = -1.84,\ \ a_{\pi\Sigma} = -2.00,\ \ a_{\pi\Lambda} = -1.83, \\ a_{\eta\Lambda} = -2.25,\ \ a_{\eta\Sigma} = -2.38,\ \ a_{K\Xi} = -2.67, \end{aligned} \tag{21}$$

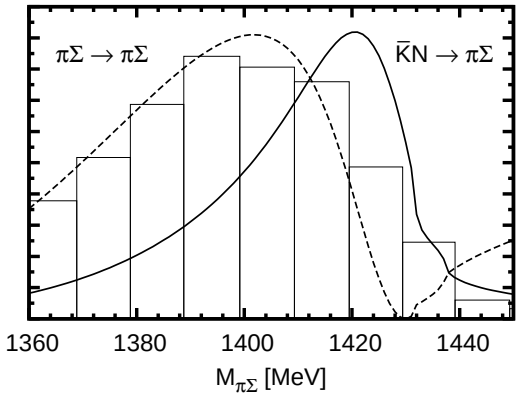

Fig. 3. $\pi\Sigma$ invariant mass spectra of two-body scatterings of $\bar{K}N \to \pi\Sigma$ (solid line) and $\pi\Sigma \to \pi\Sigma$ (dashed line) with $I = 0$ in arbitrary units. The histogram denotes an experimental data in Ref. [25].

with $\mu = 630$ MeV. The scattering amplitudes calculated with this parameter set reproduce well the $\pi\Sigma$ invariant mass spectrum and the total cross sections of K^-p to several channels [5], and the $\Lambda(1405)$ is found to be almost a purely dynamical state of meson and baryon [8].

We use the scattering amplitudes obtained in the chiral unitary approach described above for the $\bar{K}N \to \bar{K}N$ and $\bar{K}N \to \pi\Sigma$ amplitudes in Eqs. (10), (13) and (16). After fixing the subtraction parameters $a_i(\mu)$ in the two-body scattering, we have no adjustable parameters for the calculation of the $K^-p \to \pi\Sigma n$ reaction in the present approach.

The scattering amplitudes obtained in the chiral unitary approach have notable features. The $\Lambda(1405)$ is successfully reproduced by meson-baryon dynamics, but the resonance position depends on the channels [9]. In Fig. 3, we plot the $\pi\Sigma$ invariant mass distributions for $\bar{K}N \to \pi\Sigma$ and $\pi\Sigma \to \pi\Sigma$ with $I = 0$ defined by

$$\frac{d\sigma_{MB}}{dM_{\pi\Sigma}} = A|T|^2 q_{\rm c.m} \qquad (22)$$

where A is a constant, $q_{\rm c.m.}$ is the CM momentum of the final $\pi\Sigma$ state and T is the two-body meson-baryon scattering amplitude. We also show in Fig. 3, as the histogram, the experimental data of the $\pi^-\Sigma^+$ invariant mass spectrum obtained in $K^-p \to \Sigma^+\pi^-\pi^+\pi^-$ at 4.2 GeV/c for a K^- beam with the restriction of the $\Sigma^+\pi^-\pi^+$ invariant mass being between 1.6 to 1.72 GeV at which the $\Sigma(1660)$ resonance (acting as a doorway of the reaction) is located [25].

As seen in Fig. 3, the line shapes of these two channel are significantly different and the peak position in the $\pi\Sigma$ initiated scattering is 20 MeV lower than in $\bar{K}N$ scattering. This is because $\pi\Sigma$ is so strongly correlated as to produce the lower mass resonance pole in these energies[1]. As already discussed above, in the present process

[1] The importance of the strong $\pi\Sigma$ correlation in $\bar{K}N$ subthreshold scattering with $S = -1$ was recently pointed out in Ref. [27].

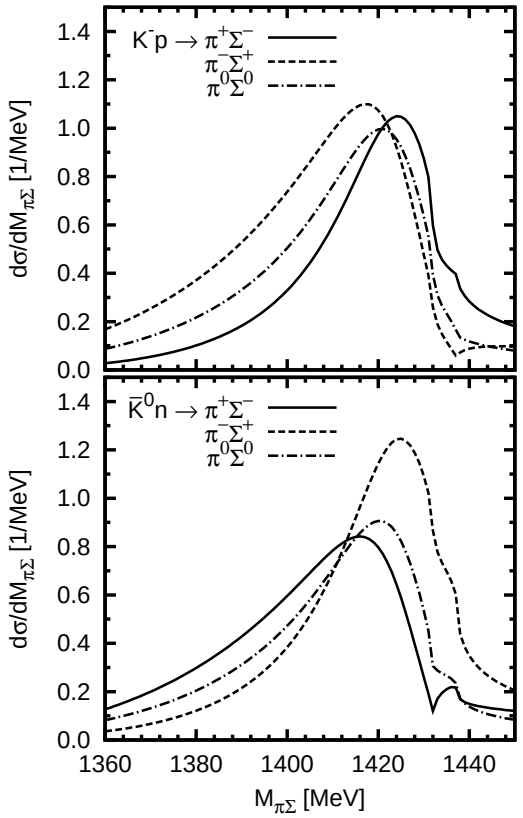

Fig. 4. $\pi\Sigma$ invariant mass spectra of two-body scatterings of $K^-p \to \pi\Sigma$ (upper panel) and $\bar{K}^0n \to \pi\Sigma$ (lower panel) for different $\pi\Sigma$ charged states. We take $A = 1$ in Eq. (22).

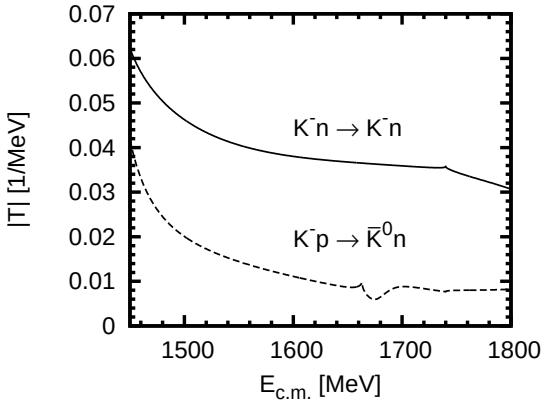

Fig. 5. Modules of $\bar{K}N$ scattering amplitude obtained in the chiral unitary approach.

$K^-d \to \Lambda(1405)n$, the $\Lambda(1405)$ is driven by the $\bar{K}N$ channel. Thus, it is expected that the $\Lambda(1405)$ spectrum shape has a peak around 1420 MeV instead of 1405 MeV.

We also remark that the $\Lambda(1405)$ line shapes are moderately different in different charged states of the π and Σ. This is simply due to the interference of $I = 0$ and $I = 1$ components in the scattering amplitudes [26]. For later convenience we show the mass spectra (22) for K^-p and $\bar{K}^0n$ to $\pi^\pm\Sigma^\mp$ and $\pi^0\Sigma^0$ in Fig. 4.

For the amplitude T_1 in Fig. 2, we plot, in Fig. 5, the modules of the $\bar{K}N$ scattering amplitudes in the relevant energy region to the present calculation. The $K^-n \to K^-n$ amplitude appearing in diagram 2 is about a factor 4 larger than $K^-p \to \bar{K}^0n$ in diagram 3 for the energy range from $E_{\rm c.m.} = 1600$ to 1800 MeV. Thus, we expect that diagram 2 gives a larger contribution than diagram 3 for the incident K^- momenta from 600 to 1000 MeV/c. The dip structure around 1670 MeV in $K^-p \to \bar{K}^0n$ is due to the presence of the $\Lambda(1670)$ resonance with $I = 0$, while $K^-n \to K^-n$ has purely $I = 1$ and there is no structure for the $\Lambda(1670)$.

3 Results

In this section, we show the numerical results of the calculations for the $K^-d \to \pi\Sigma n$ reaction. The $\pi\Sigma$ invariant mass is calculated by integrating the differential cross section (1) with respect to the angles of the final pion and neutron:

$$\frac{d\sigma}{dM_{\pi\Sigma}} = \frac{M_d M_\Sigma M_n}{(2\pi)^3\, 2k_{\rm c.m.} E^2_{\rm c.m.}} \int |\mathcal{T}|^2 |\boldsymbol{p}^*_\pi|\, |\boldsymbol{p}_n|\, d\cos\theta \quad (23)$$

where θ is the scattering angle of the neutron in the c.m. frame. The integrals in terms of the pion solid angle and neutron azimuth can be performed, since the amplitude is not dependent on these angles. The T-matrix $\mathcal{T}$ is evaluated as a sum of the amplitudes given in Eqs. (10), (13) and (16). These amplitudes contain two-body meson-baryon scattering amplitudes of $\bar{K}N \to \bar{K}N$ and $\bar{K}N \to \pi\Sigma$. These amplitudes are calculated in the chiral unitary approach described in Sec. 2.3. The $\bar{K}N \to \bar{K}N$ scattering amplitudes are functions of the c.m. energy of the incident kaon and one of the nucleons in the deuteron, which can be determined when the initial kaon momentum is fixed, as discussed in Eq. (15), while the $\bar{K}N \to \pi\Sigma$ amplitudes are functions of the $\pi\Sigma$ invariant mass $M_{\pi\Sigma}$ and provide the resonance shape for the $\Lambda(1405)$.

3.1 Comparison with the experimental data of $K^-d \to \pi^+\Sigma^-n$

First of all, we compare our theoretical calculation of the $K^-d \to \pi^+\Sigma^-n$ reaction with the experimental data reported in Ref. [28]. The experiment was performed with K^- having momenta between 686 and 844 MeV/c and the particles were detected by bubble chamber.

3.1.1 $\pi^+\Sigma^-$ invariant mass spectrum

We show, in Fig. 6, the $\pi^+\Sigma^-$ invariant-mass spectrum in arbitrary units at 800 MeV/c incident K^- momentum and compare our theoretical calculation with the experimental data. The data are taken from the bubble chamber experiment at K^- momenta between 686 and 844 MeV/c [28]. In the analysis of this experiment, the resonance contribution was determined by fitting a relativistic Breit-Wigner distributions and a smooth background parametrized as a sum of Legendre polynomials to the data. We show, in Fig. 6, the resonance (foreground) contributions for the experimental data which are obtained by subtracting the background contributions estimated with the Legendre polynomials in Ref. [28] from the actual data points given in the paper. The solid line denotes our theoretical calculation with the chiral unitary approach.

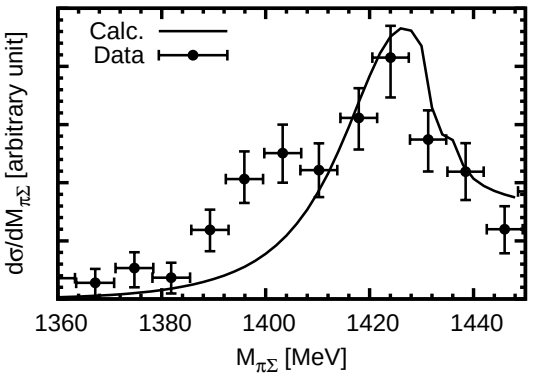

Fig. 6. $\pi\Sigma$ invariant mass spectra of $K^-d \to \pi^+\Sigma^-n$ in arbitrary units at 800 MeV/c incident K^- momentum. The solid line denotes the present calculation. The data are taken from the bubble chamber experiment at K^- momenta between 686 and 844 MeV/c given in Ref. [28].

The spectrum shape obtained in this calculation agrees with that of the experimental observation. Especially it is very interesting to see that the peak position, which comes from the $\Lambda(1405)$ production, appears around $M_{\pi\Sigma} = 1420$ MeV instead of 1405 MeV announced nominally by the Particle Data Group. This is one of the strongest evidences that the resonance position of the $\Lambda(1405)$ depends on the initial channel of meson and baryon, and supports the double pole nature of the $\Lambda(1405)$, in which the higher state sitting in 1420 MeV strongly couples to the $\bar{K}N$ channel.

The bump structure seen around $M_{\pi\Sigma} = 1390$ MeV is probably related to the p-wave contributions coming from the $\Sigma^*(1385)$ production, which we did not take into account in the present calculation. Let us estimate a possible influence of the $\Sigma(1385)$ resonance on the $\Lambda(1405)$ spectrum appearing around 1420 MeV. We calculate the $\Sigma(1385)$ spectrum in the Breit-Wigner formulation with the mass 1385 MeV and the width 37 MeV including the phase space factor $|\boldsymbol{p}^*_\pi|\, |\boldsymbol{p}_n|$ as seen in Eq. (23). Summing up the spectra of the $\Lambda(1405)$ and $\Sigma(1385)$ incoherently, we find that the peak structure at 1420 MeV is not affected by the $\Sigma(1385)$ contribution as seen in Fig. 7 (dash-dotted line). In this estimation, we have adjusted the height of the $\Sigma(1385)$ spectrum so as to reproduce the observed bump structure around 1390 MeV. For further quantitative calculations of the $\Sigma(1385)$ spectrum, we would have to take into account of the $\Sigma(1385)$ production mechanism in the present reaction and sum the amplitudes coherently, which could be done by including the p-wave contributions with

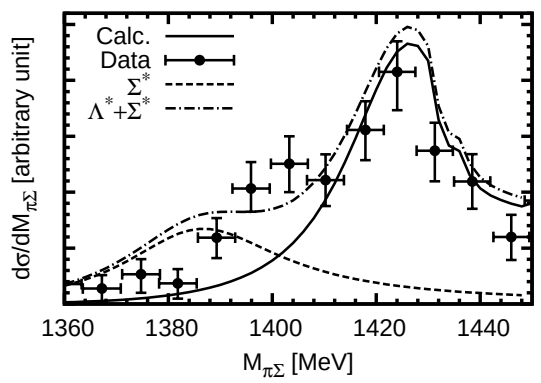

Fig. 7. A possible inference of the $\Sigma(1385)$ resonance to the $\Lambda(1405)$ spectrum of $K^- d \to \pi^+ \Sigma^- n$ at 800 MeV/c incident K^- momentum. The $\Sigma(1385)$ spectrum (dashed line) is calculated by the Breit-Wigner amplitude and the phase space factor $|\boldsymbol{p}_\pi^*|\,|\boldsymbol{p}_n|$. The dash-dotted lines denotes an incoherent sum of the $\Lambda(1405)$ and $\Sigma(1385)$ spectrum. The height of the $\Sigma(1385)$ spectrum is adjusted so as to reproduce the bump structure around 1390 MeV in the observed spectrum. See also the caption of Fig. 6.

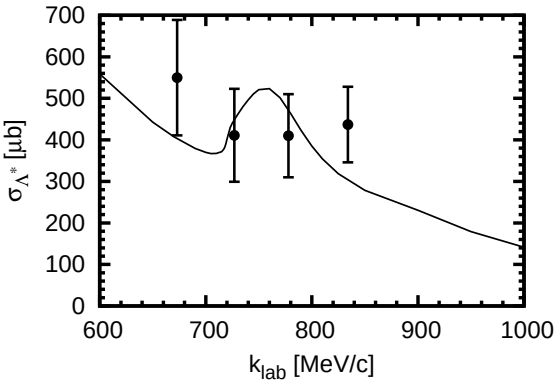

Fig. 8. Incident K^- momentum dependence of the $\Lambda(1405)$ production cross section calculated with the $K^- d \to \pi^+ \Sigma^- n$ reaction. The data are taken from Ref. [28].

the $\Sigma(1385)$ resonance in the present formulation of the two-body meson-baryon scattering amplitudes $T_{\bar{K}N\to\pi\Sigma}$ following Ref. [29]. Because in angular integrated cross sections the interference of s- and p-waves disappears, the incoherent sum done here should be good and the relevant finding for the present work is that consideration of the $\Sigma(1385)$ contribution does not distort the signal of the $\Lambda(1405)$ that we find.

Since the purpose of the paper is to show that the peak around 1420 MeV is a reflection of the $\Lambda(1405)$ and is narrower than for the nominal $\Lambda(1405)$, we have done an alternative study assuming the shape of Fig. 7 to be made by two Breit Wigner distributions that add incoherently. A fit of excellent quality is obtained and the structure peaking around 1420 MeV is very similar to what we obtain theoretically from the $\Lambda(1405)$. A best fit with only one Breit Winger structure, obviously does not reproduce the peak at lower energies in Fig. 7 and is of lower quality than that of the two structures. Even then, it is interesting to mention that the peak of this only structure is still around 1420 MeV.

3.1.2 Λ^* production cross section

We also estimate the production cross section of the $\Lambda(1405)$ in the $K^- d \to \Lambda(1405) n$ reaction by integrating the spectrum obtained in our calculation over the $\pi\Sigma$ invariant mass around the resonance peak:

$$\sigma_{\Lambda^*} = 3 \int_{M_{\rm min}}^{M_{\rm max}} dM_{\pi^+\Sigma^-} \frac{d\sigma}{dM_{\pi^+\Sigma^-}} \ . \qquad (24)$$

The factor 3 accounts for the branching ratio of $\Lambda(1405) \to \pi^+\Sigma^-$. Taking $M_{\rm min} = 1400$ MeV and $M_{\rm max} = 1440$ MeV read from the figure, we obtain the $\Lambda(1405)$ production cross section as 385 μb with 800 MeV/c incident K^-. An experimental value observed in the $K^- d \to \pi^+\Sigma^- n$ reaction is reported to be 410$\pm$100 μb at 778 MeV/c of the incident K^- momentum [28]. The present calculation fairly agrees with the observed value. This implies that the $\Lambda(1405)$ production mechanism in the present reaction is explained by the three diagrams shown in Fig. 2.

In Fig. 8, we show the incident momentum dependence of the $\Lambda(1405)$ production cross section. The cross sections are evaluated from the $K^- d \to \pi^+\Sigma^- n$ channel by integrating the invariant mass spectra from 1400 MeV to 1440 MeV and multiplying by the isospin factor 3. The experimental data are taken again from Ref. [28]. Our calculation is consistent with the experimental data. The bump structure seen in the theoretical calculation around $k_{\rm lab} = 750$ MeV/c corresponds to the $\Lambda(1670)$ resonance production in the T_1 amplitude of $K^- p \to \bar{K}^0 n$ (see Fig. 2) [2].

3.2 Theoretical results of the $\pi\Sigma$ invariant mass spectra

3.2.1 Spectra of other $\pi\Sigma$ charged states

In the previous section, we have seen that the $\Lambda(1405)$ resonance appears around 1420 MeV in the $\pi^+\Sigma^-$ invariant mass spectrum. To confirm that the resonance position of the $\Lambda(1405)$ in the $\bar{K}$ induced processes is higher than the nominal $\Lambda(1405)$, it is certainly necessary to project out the $I = 0$ contributions from the invariant mass spectra, since the shift of the resonance position could be explained by interference between the $I = 0$ $\Lambda(1405)$ resonance and non-resonant $I = 1$ $\pi\Sigma$ correlations.

[2] The bump structure could be less pronounced with corrections to the factorization approximation of the $T_{K^- N\to\bar{K}N}$ amplitude for the double scattering diagrams done in Eqs. (13) and (16). For the details, see Sec. 3.2.5.

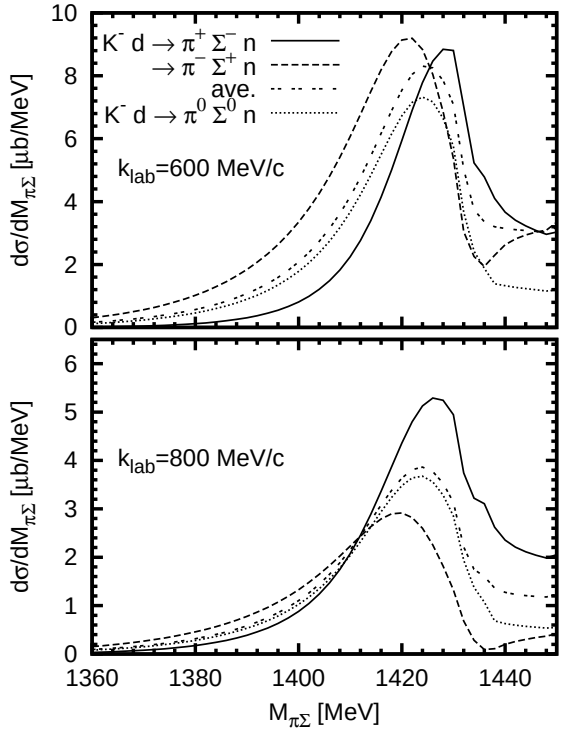

Fig. 9. $\pi\Sigma$ invariant mass spectra of $K^- d \to \pi\Sigma n$ with different charged $\pi\Sigma$ states. The solid, dashed and dotted lines denote the invariant mass spectra of $\pi^+\Sigma^-$, $\pi^-\Sigma^+$ and $\pi^0\Sigma^0$ for the final $\pi\Sigma$ state, respectively. The double-dotted line shows the averaged spectrum of $\pi^+\Sigma^-$ and $\pi^-\Sigma^+$ of the final $\pi\Sigma$ states.

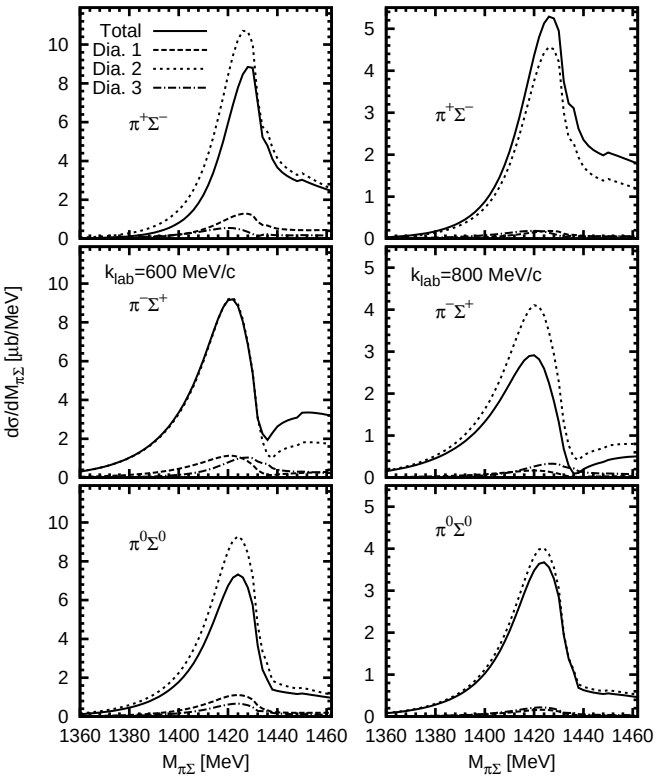

Fig. 10. $\pi\Sigma$ invariant mass spectra of $K^- d \to \pi\Sigma n$ separately plotted in each diagram contribution. The solid line denotes the total contributions of three diagrams. The dashed, dotted and dash-dotted lines show the calculations from diagram 1, 2 and 3 shown in Fig. 2, respectively. The plots in the left and right panels are calculated with 600 and 800 MeV/c of K^- incident momenta, respectively. The charge states of $\pi\Sigma$ are shown in the plots.

In Fig. 9, we plot the $\pi\Sigma$ invariant mass spectra for the different charged $\pi\Sigma$ states with incident K^- momenta of 600 and 800 MeV/c. We also plot the averaged spectrum of $K^- d \to \pi^+\Sigma^- n$ and $K^- d \to \pi^-\Sigma^+ n$, in which interference terms of $I = 0$ and $I = 1$ in the $\pi\Sigma$ correlation are cancelled out. In the spectrum of $K^- d \to \pi^0\Sigma^0 n$, there are not $I = 1$ contributions in the $\pi\Sigma$ system.

The peak positions are slightly dependent on the charged channels due to the interference between the $\Lambda(1405)$ resonance with $I = 0$ and non-resonant $\pi\Sigma$ scattering with $I = 1$. The differences are within several MeV. The peak positions are insensitive to the incident K^- momenta, but the heights are dependent on the K^- momenta. This is because the contribution from each diagram depends on the incident momentum and interference between the diagrams shown in Fig. 2 makes the heights of the spectrum dependent on the incident momentum.

3.2.2 Contributions from each diagram

In Fig. 10 we show the $\pi\Sigma$ invariant mass spectra with separated contributions from the diagrams shown in Fig.2. In the diagram 1, the $\Lambda(1405)$ resonance is created by the incident K^- and the proton inside the deuteron, and the neutron is a spectator of the $\Lambda(1405)$ production. In the diagrams 2 and 3, two nucleons contribute the $\Lambda(1405)$ production with one kaon exchange. In Fig. 10, we find that the diagram 2 gives the dominant contribution to the total spectrum and that the impulse approximation diagram 1 is negligible, specially at higher incident momenta. The reason why the two-nucleon processes give large contributions can be understood as follows. In the present reaction the $\Lambda(1405)$ is produced by the $\bar{K}N$ channel below its threshold. Thus, some amount of energy should be taken out by the final neutron with energy transfer between the nucleons. In the double scattering processes (diagrams 2 and 3), the transferred energy is taken from the initial kaon, such that the exchanged kaon carries less energy than on shell. In the impulse process of the diagram 1, the energy should be transferred by the relative motion of the nucleons inside the deuteron. Due to the small binding energy of the deuteron, the deuteron wavefunction has small high energy components. Therefore, the contribution of the diagram 1 is negligibly small. The reason that the diagram 3 is relatively smaller than diagram 2 is that the s-wave $K^- p \to \bar{K}^0 n$ amplitude in the diagram 3 is smaller than the $K^- n \to K^- n$ in the diagram 2 at the present energy region as seen in Fig. 5.

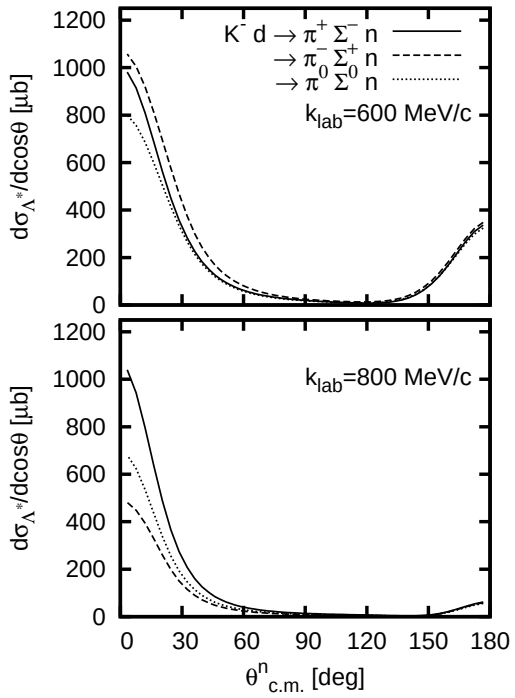

Fig. 11. Angular dependence of the $\Lambda(1405)$ production cross section. The horizontal axis is the angle between the incident kaon and the emitted neutron in center of mass frame. The incident K^- momenta are 600 MeV/c and 800 MeV/c in the upper and lower panels, respectively.

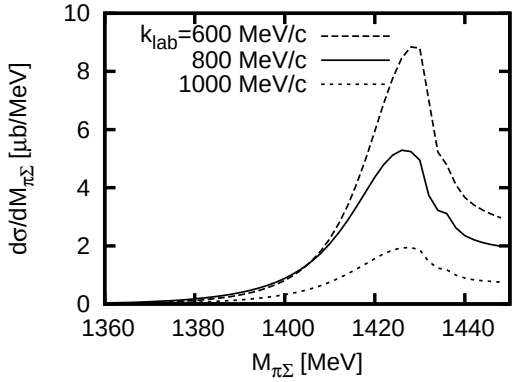

Fig. 12. $\pi\Sigma$ invariant mass spectra of the $K^-d \to \pi^+\Sigma^-n$ reaction with 600, 800 and 1000 MeV/c incident K^- momenta.

3.2.3 Angular dependence of the $\Lambda(1405)$ production cross section

In Fig. 11, we plot the angular dependence of the $\Lambda(1405)$ production cross section of a function of the angle of the incident kaon and the outgoing neutron in the center of mass frame. The differential cross section is calculated by

$$\frac{d\sigma_{\Lambda^*}}{d\cos\theta} = \int_{M_{\rm min}}^{M_{\rm max}} dM_{\pi\Sigma} \frac{d\sigma}{dM_{\pi\Sigma} d\cos\theta} \qquad (25)$$

with $M_{\rm min} = 1400$ MeV and $M_{\rm max} = 1440$ MeV. Here we do not multiply by a factor 3, since we consider the production cross section of each final $\pi\Sigma$ state.

There are two contributions for the $\Lambda(1405)$ production. One is backward Λ^* production ($\theta^n_{\rm c.m.} \simeq 0^\circ$) and the other one is forward production ($\theta^n_{\rm c.m.} \simeq 180^\circ$). Figure 11 shows that large contributions to the total $\Lambda(1405)$ production come from the backward production.

The forward Λ^* production with $\theta^n_{\rm c.m.} > 150^\circ$ comes from diagram 1 in Fig. 2. As already mentioned, in this diagram the neutron inside the deuteron can be regarded as a spectator of the $\Lambda(1405)$ production from K^-p. Therefore the neutron goes to the backward angles $\theta^n_{\rm c.m.} > 150^\circ$. On the other hand, in the double scattering processes (diagram 2 and 3), the energetic incident kaon kicks one of the nucleons in the deuteron to forward directions and the exchanged kaon goes to backward angles. The recoil momentum depends on the emitted nucleon angles and gets smaller with larger recoil angles. The exchanged kaon going backward produces the $\Lambda(1405)$ together with the other nucleon in the deuteron. Since the momentum distribution of the nucleons in the deuteron is concentrated at low momenta, less than 100 MeV/c, a good momentum matching to create the $\Lambda(1405)$ is achieved by small momenta of the exchanged kaon, namely large momentum transfer of the incident K^- to the emitted neutron. Therefore, in the double scattering processes, the production rate of the $\Lambda(1405)$ is dominated by the backward angles.

3.2.4 Incident K^- momentum dependence

As we have already shown in Fig. 8, the $\Lambda(1405)$ production cross section in $K^-d \to \pi^+\Sigma^-n$ decreases as the incident K^- momentum increases. This is because more energetic incident K^- produce the $\Lambda(1405)$ less efficiently due to worse momentum matching between the kaons and the nucleons inside the deuteron in both direct production (diagram 1) and double scattering (diagram 2 and 3) processes.

In Fig. 12, we show the incident momentum dependence of the $\pi\Sigma$ invariant spectra of the $K^-d \to \pi^+\Sigma^-n$ reaction. We find that the height of the resonance peak for the $\Lambda(1405)$ around 1420 MeV has a strong incident momentum dependence, as seen in the production cross section, but the spectrum shapes do not depend on the incident energy.

For lower momenta of the incident K^-, since the production cross sections of the $\Lambda(1405)$ are enhanced, one would expect some advantage to observe the $\Lambda(1405)$ using low energy incident K^-. This is true for not very low momenta of the incident K^-. For instance, we plot the $\pi\Sigma$ invariant mass spectra at 400 MeV/c incident K^- momentum in the right panel of Fig. 13. These figures show that the heights of the spectra are about five times larger than those of the spectra obtained with 600 MeV/c of the incident K^-, and that the spectrum shapes are very similar to

each other. Thus, using 400 MeV/c incident K^- is better to observe the $\Lambda(1405)$ spectra. It is also seen that diagram 1 and 3 give a moderate contribution to the spectra, as seen in Fig. 13. We show also the angular dependence of the $\Lambda(1405)$ production cross sections in Fig. 14. Due to the substantial contribution from diagram 1, which is the single step process, the $\Lambda(1405)$ is produced also at forward angles.

For further low incident momenta, the spectra can be distorted by threshold effects. We show the $\pi\Sigma$ invariant mass spectra for the 200 MeV/c incident K^- in the left panel of Fig. 13. As seen in Fig. 13 for the $\pi^+\Sigma^-$ spectrum, the signal of the $\Lambda(1405)$ production is distorted by the strong contributions around 1440 MeV. This peak structure is produced by a threshold effect and has nothing to do with any resonances. The phase space is given by the neutron momentum in the c.m frame of the reaction and the pion momentum in the rest frame of π and Σ. The maximum invariant mass $M_{\pi\Sigma}$ for the 200 MeV/c incident K^- is at 1460 MeV. At the maximum invariant mass, the neutron momentum becomes zero, while the pion momentum has a maximum value. Because these two factors compete below the threshold, the phase space suppression is slow and shows up only at the invariant mass very close to the threshold. This creates the peak structure. For the incident momentum of 200 MeV/c, diagram 1 gives the dominant contributions, as seen in Fig. 13. This has as a consequence that most of the $\Lambda(1405)$ is produced at forward angles (See Fig. 14).

For incident K^- momenta smaller than 200 MeV/c, the maximum invariant mass of $\pi\Sigma$ in the $K^-d \to \pi\Sigma n$ reaction approaches that of the $\Lambda(1405)$ and the signal for this resonance becomes unclear. Thus, it is hard to investigate the $\Lambda(1405)$ properties in this reaction with incident K^- momenta smaller than 200 MeV/c.

It is important to discuss two particular cases where the experiment is likely to be suggested. One of them is the case of kaons at rest, which are often used in many other experiments. The other one is the case of kaons coming from ϕ decay, which are used at FINUDA in the Frascati facility. We have performed the calculations for these two cases, in the first one using kaons of 5 MeV/c instead of stopped kaons, and in the second case using kaons of 120 MeV/c. The results can be seen in Fig. 15. For the low momentum case we observe the dominance of the impulse approximation term, giving a large contribution close to threshold which extends below threshold due to Fermi motion. The important thing to see is that the impulse approximation term is absolutely dominant and the trace of the $\Lambda(1405)$ is lost in the figure. One can certainly conclude that the case of stopped kaons does not provide a good set up to learn about the $\Lambda(1405)$. On the other hand the situation for the Frascati Laboratory is also not very promissing. Although a signal of the $\Lambda(1405)$ can be seen, the contribution of the impulse approximation term is too large and distorts the signal of the resonance which is more clearly seen at higher energies.

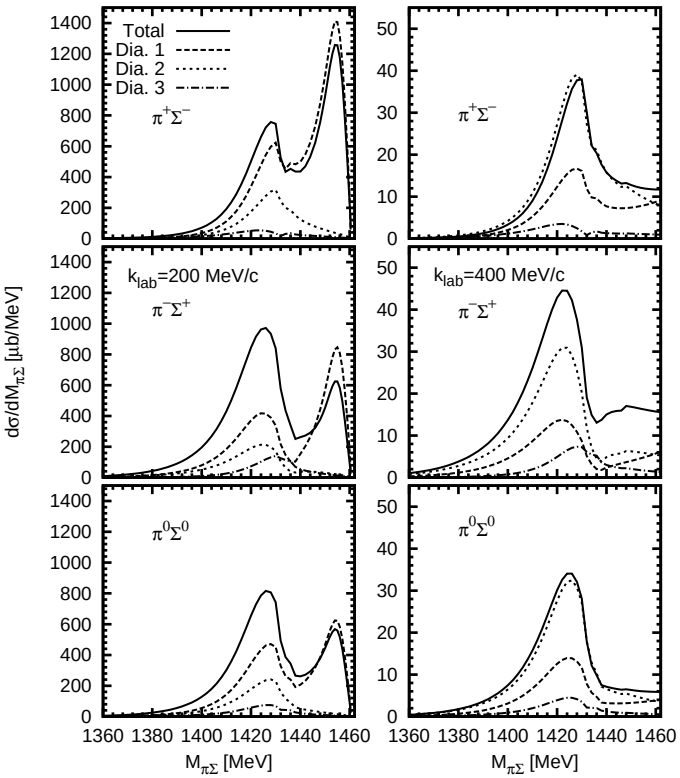

Fig. 13. $\pi\Sigma$ invariant mass spectra of $K^-d \to \pi\Sigma n$ separately plotted in each diagram contribution. The plots in the left and right panels are calculated with 200 and 400 MeV/c of K^- incident momenta, respectively. Same as described in the caption to Fig. 10.

3.2.5 Validity of the approximation of fixing the energy of the $T_{K^-N\to\bar{K}N}$ amplitude in Eqs. (13) and (16).

In the present work, we have calculated the $\Lambda(1405)$ spectra under the assumption that the amplitude $T_{K^-N\to\bar{K}N}$ in the double scattering processes, diagram 2 and 3 in Fig. 2, is factorized from the momentum integral by fixing the invariant energy of the scattering amplitude as Eq. (15). This may be a good approximation if the amplitude $T_{K^-N\to\bar{K}N}$ does not change so much in the relevant momentum range of the integral, which is determined by the deuteron wavefunction. Inclusion of the integral momentum dependence to the scattering amplitude is expected not to affect the shape of the $\pi\Sigma$ invariant mass spectrum, since the spectral shape is determined by the $\bar{K}N \to \pi\Sigma$ scattering amplitude and its energy is fixed by the final state. Here we show a calculation performed with the integral momentum dependence in the amplitude $T_{K^-N\to\bar{K}N}$ to see the validity of the approximation.

In Fig. 16, we show the $\pi\Sigma$ invariant mass spectra of $K^-d \to \pi^+\Sigma^-n$ with the 800 MeV/c incident K^- calculated without and with the integral momentum dependence of the $T_{K^-N\to\bar{K}N}$ amplitude in the double scattering diagrams. The calculation (the solid line) without the momentum dependence of the $K^-N \to \bar{K}N$ amplitude is the same as in the previous calculations. The momentum

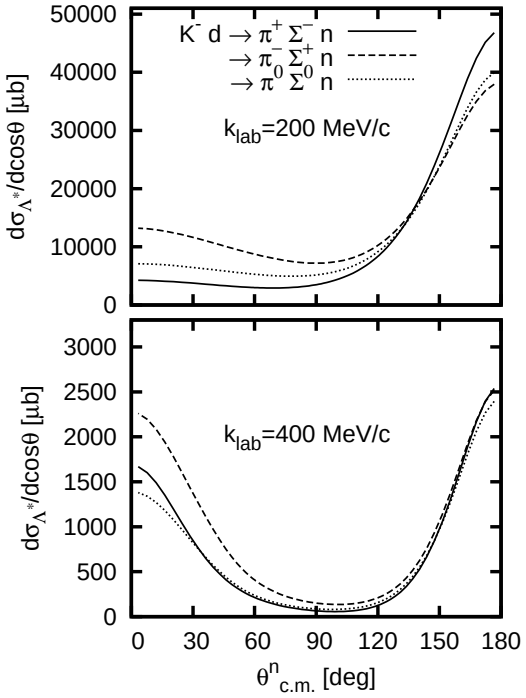

Fig. 14. Angular dependence of the $\Lambda(1405)$ production cross section for the incident K^- momenta of 200 MeV/c and 400 MeV/c in the upper and lower panels, respectively. Same as described in the caption to Fig. 11.

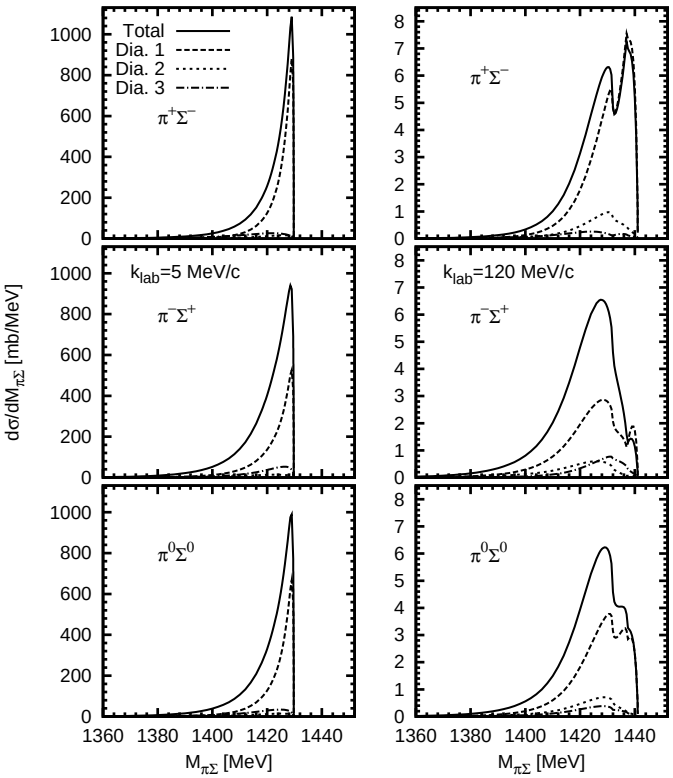

Fig. 15. $\pi\Sigma$ invariant mass spectra of $K^-d \to \pi\Sigma n$ separately plotted in each diagram contribution. The plots in the left and right panels are calculated with 5 and 120 MeV/c of K^- incident momenta, respectively. Same as described in the caption to Fig. 10.

dependence on the energy of the $\bar{K}N \to \pi\Sigma$ scattering amplitude has been included by

$$W_1 = \sqrt{(k^0 + M_N)^2 - (\boldsymbol{q} + \boldsymbol{p}_n)^2} \tag{26}$$

The dotted line of Fig. 16 denotes the spectrum obtained by the inclusion of the momentum dependence. As seen in Fig. 16, the difference between the two lines is small and the spectral shapes are very similar. The strength of the spectra is slightly different. This is because, for the 800 MeV/c incident K^-, W_1 can be 1700 MeV with the nucleon in the deuteron at rest, and the scattering amplitude $T_{K^-N\to\bar{K}N}$ has small energy dependence around this energy as seen in Fig. 5. Thus, our conclusion that the $\pi\Sigma$ mass spectra have a peak for the $\Lambda(1405)$ around 1420 MeV in the $K^-d \to \pi\Sigma n$ reaction does not change at all even if we include the momentum dependence into the $K^-N \to \bar{K}N$ amplitude.

For the absolute value of the production of the $\Lambda(1405)$ in the present reaction, we could have 5% to 25 % corrections depending on the K^- incident momentum from the approximation of the loop momentum integral. For instance, in case of the 750 MeV/c incident K^-, W_1 can be around 1650 MeV where the $K^-p \to \bar{K}^0n$ amplitude has a bump caused by the presence of the $\Lambda(1670)$ resonance (see Fig. 5). Due to the strong energy dependence of the $K^-p \to \bar{K}^0n$ amplitude around $W_1 \simeq 1650$ MeV, we found the correction to be 25 % in the absolute value. The main consequence of this correction is that the

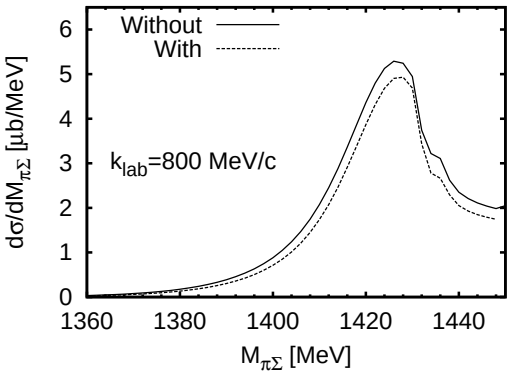

Fig. 16. $\pi\Sigma$ invariant mass spectra of $K^-d \to \pi^+\Sigma^-n$ with the 800 MeV/c incident K^- calculated without and with the integral momentum dependence of the $T_{K^-N\to\bar{K}N}$ amplitude in the double scattering diagrams. The solid line denotes the calculation without the momentum dependence of the $K^-N \to \bar{K}N$ amplitude, which is the same as in the previous calculations. The dotted line is the spectrum obtained by the inclusion of the momentum dependence.

bump structure seen in the $\Lambda(1405)$ cross section around $k_{\rm lab} \sim 750$ MeV/c in Fig. 8 is smeared out and the energy dependence of the integrated cross section is now smoother.

4 Summary

We have studied the K^- induced production of $\Lambda(1405)$ with a deuteron target by calculating the observable $K^- d \to \pi\Sigma n$ reaction. We have found that, in the $K^- d \to \pi\Sigma n$ process, the $\Lambda(1405)$ resonance is produced by the $\bar{K}N$ channel, and, therefore, this process is suited to investigate the properties of the $\Lambda(1405)$ induced by subthreshold $\bar{K}N$.

We have calculated the $\pi\Sigma$ invariant mass spectra of the $K^- d \to \pi\Sigma n$ reaction using the $\bar{K}N \to \bar{K}N$ and $\bar{K}N \to \pi\Sigma$ amplitudes obtained by the chiral unitary approach. The present calculation agrees with the observed spectrum of $K^- d \to \pi^+\Sigma^- n$ in the bubble chamber experiment, in which the $\Lambda(1405)$ resonance appears at 1420 MeV not 1405 MeV. The present model also reproduces the $\Lambda(1405)$ production cross section. We have also found that the $\Lambda(1405)$ production has a strong angular dependence in this reaction and that the $\Lambda(1405)$ is produced mostly in backward directions against the incident K^-. We have shown that the production cross section decreases as the incident K^- momentum increases. Due to the worse momentum matching between the kaon and the nucleon inside the deuteron, the more energetic incident K^-s produce less $\Lambda(1405)$s. These findings should be a guideline for future experiments that would help understand the dynamics and repercussions of subthreshold $\bar{K}N$ production of the $\Lambda(1405)$.

Acknowledgements

This work was partly supported by the Grant-in-Aid for Scientific Research from MEXT and JSPS (Nos. 20028004 and 20540273), the collaboration agreement between the JSPS of Japan and the CSIC of Spain, and the Grant-in-Aid for the Global COE Program "The Next Generation of Physics, Spun from Universality and Emergence" from MEXT of Japan. This work was also supported in part by DGICYT contract number FIS2006-03438. We acknowledge the support of the European Community-Research Infrastructure Integrating Activity "Study of Strongly Interacting Matter" (acronym HadronPhysics2, Grant Agreement n. 227431) under the Seventh Framework Programme of EU. Work supported in part by DFG (SFB/TR 16, "Subnuclear Structure of Matter"). This work was done under the Yukawa International Program for Quark-hadron Sciences (YIPQS).

References

1. R. H. Dalitz, T. C. Wong and G. Rajasekaran, Phys. Rev. **153**, 1617 (1967).
2. N. Kaiser, P. B. Siegel, and W. Weise, Nucl. Phys. **A594**, 325 (1995).
3. E. Oset and A. Ramos, Nucl. Phys. **A635**, 99 (1998).
4. J. A. Oller and U. G. Meissner, Phys. Lett. **B500**, 263 (2001).
5. E. Oset, A. Ramos, and C. Bennhold, Phys. Lett. **B527**, 99 (2002).
6. C. Garcia-Recio, J. Nieves, E. Ruiz Arriola and M. J. Vicente Vacas, Phys. Rev. D **67**, 076009 (2003).
7. T. Hyodo, S. I. Nam, D. Jido, and A. Hosaka, Phys. Rev. C **68**, 018201 (2003); Prog. Theor. Phys. **112**, 73 (2004).
8. T. Hyodo, D. Jido and A. Hosaka, Phys. Rev. C **78**, 025203 (2008).
9. D. Jido, J. A. Oller, E. Oset, A. Ramos and U. G. Meissner, Nucl. Phys. A **725**, 181 (2003).
10. T. Hyodo, A. Hosaka, M. J. Vicente Vacas and E. Oset, Phys. Lett. B **593**, 75 (2004).
11. J. C. Nacher, E. Oset, H. Toki and A. Ramos, Phys. Lett. B **461**, 299 (1999).
12. S. Prakhov *et al.* [Crystall Ball Collaboration], Phys. Rev. C **70**, 034605 (2004).
13. V. K. Magas, E. Oset and A. Ramos, Phys. Rev. Lett. **95**, 052301 (2005).
14. T. Kishimoto, Phys. Rev. Lett. **83**, 4701 (1999).
15. C. Amsler *et al.* [Particle Data Group], Phys. Lett. B **667**, 1 (2008).
16. M. Lacombe, B. Loiseau, R. Vinh Mau, J. Cote, P. Pires and R. de Tourreil, Phys. Lett. B **101**, 139 (1981).
17. G. Toker, A. Gal and J. M. Eisenberg, Nucl. Phys. A **362**, 405 (1981).
18. M. Torres, R. H. Dalitz and A. Deloff, Phys. Lett. B **174**, 213 (1986).
19. A. Bahaoui, C. Fayard, G. H. Lamot and T. Mizutani, Nucl. Phys. A **508**, 335c (1990).
20. S. S. Kamalov, E. Oset and A. Ramos, Nucl. Phys. A **690**, 494 (2001).
21. J. Nieves, E. Oset and C. Garcia-Recio, Nucl. Phys. A **554**, 554 (1993).
22. L. L. Salcedo, E. Oset, M. J. Vicente-Vacas and C. Garcia-Recio, Nucl. Phys. A **484**, 557 (1988).
23. R. Machleidt, Phys. Rev. C **63**, 024001 (2001).
24. D. N. Tovee *et al.*, Nucl. Phys. B **33**, 493 (1971); R. J. Nowak *et al.*, *ibid.* **139**, 61 (1978).
25. R. J. Hemingway, Nucl. Phys. B **253**, 742 (1985).
26. J. C. Nacher, E. Oset, H. Toki and A. Ramos, Phys. Lett. B **455**, 55 (1999).
27. T. Hyodo and W. Weise, Phys. Rev. C **77**, 035204 (2008).
28. O. Braun *et al.*, Nucl. Phys. B **129**, 1 (1977).
29. D. Jido, E. Oset and A. Ramos, Phys. Rev. C **66**, 055203 (2002).